INORGANIC CHEMISTRY FRONTIERS

RESEARCH ARTICLE

View Article Online
View Journal | View Issue

Cite this: *Inorg. Chem. Front.*, 2025, **12**, 7637

Stabilizing $NH_4V_4O_{10}$ by Al-doping: boosting kinetics and ammonium retention for practical zinc-ion batteries

Yuqi Peng,[a,b] Li'e Mo,*[a,b] Weilin Yan,[a,b] Lufan Liu,[a,b] Xuejun Zhu,[a,b] Yang Huang,[a,b] Zhaoqian Li,[b] Hong Zhang*[c] and Linhua Hu *[a,b]

Layered ammonium vanadate ($NH_4V_4O_{10}$) cathodes demonstrate high capacity and rapid ion transport due to their low molecular weight and open framework structure. However, practical application is hindered by strong electrostatic interactions between Zn^{2+} and V–O bonds, as well as structural instability arising from weak N–H···O bonding. To overcome these limitations, an Al^{3+} doping $NH_4V_4O_{10}$ (Al-NVO) cathode has been designed to stabilize the layered framework and achieve high-performance aqueous zinc-ion batteries (AZIBs). The incorporation of Al^{3+} ions and structural water molecules synergistically enhances Zn^{2+}–V–O binding strength while constructing additional ion diffusion channels. Pre-intercalated Al^{3+} not only acts as pillars to enhance the stability of the layered structure but also suppresses irreversible deammoniation during cycling, thereby achieving exceptional long-term stability. Density functional theory (DFT) calculations reveal that Al-NVO optimizes the electron distribution and provides a low-energy-barrier pathway for Zn^{2+} migration (0.82 eV *vs.* 1.98 eV in $NH_4V_4O_{10}$). Benefiting from these merits, the Al-NVO cathode delivers a high specific capacity of 460 mAh g^{-1} at 0.2 A g^{-1} and 94.6% capacity retention after 2000 cycles at 5 A g^{-1}. Moreover, the Al-NVO-based pouch cell exhibits a capacity of 167 mAh g^{-1} with 250-cycle stability, while a 0.6 Ah prototype battery sustains >300 h operation under deep cycling conditions, demonstrating practical feasibility for aqueous zinc-ion storage systems.

Received 9th June 2025,
Accepted 31st July 2025

DOI: 10.1039/d5qi01280e

rsc.li/frontiers-inorganic

1. Introduction

Aqueous zinc-ion batteries (AZIBs) have emerged as a promising candidate for large-scale energy storage, especially in smart grid applications.[1–3] Their attractiveness stems from the divalency and abundance of zinc, coupled with the use of aqueous electrolytes, which provide inherent safety, low cost, and substantial energy capacity.[4–6] However, compared to commercialized battery technologies, AZIBs still encounter substantial obstacles on the path to widespread adoption. These challenges primarily revolve around performance optimization, material compatibility, and long-term stability.[7–9] Specifically, the cathode material as a crucial component in AZIBs remains a major bottleneck. To fully exploit the theoretically higher capacity enabled by zinc's divalency, the cathode material must possess reasonable rate capability, high specific capacity, and superior cycling stability.[10–12]

Layered vanadium-based oxides have become one of the most promising materials for AZIB cathodes, attributed to their multiple valence states and diverse open frameworks.[13–17] Strategies such as introducing pillar ions (*e.g.*, Li^+, Na^+, K^+, Ca^{2+}, Zn^{2+}) or molecules (*e.g.*, C_3N_4, imidazole) into the structures of these oxides can effectively expand the layer spacing.[18–25] This expansion facilitates ion diffusion kinetics and enhances cycle stability. In this context, the ammonium ion (NH_4^+), characterized by its low molecular weight (18 g mol^{-1}) and large ion radius (1.43 Å), has drawn significant attention, exemplified by compounds such as $NH_4V_3O_8$, $NH_4V_4O_{10}$, $(NH_4)_2V_{10}O_{25}$, and $(NH_4)_2V_6O_{16}$.[26–29] Nevertheless, ammonium-based vanadium cathodes face two primary challenges for practical applications. First, the strong electrostatic interaction between Zn^{2+} and V–O bonds impedes the reversible de/intercalation of Zn^{2+}. Second, the weak N–H···O hydrogen bonding and irreversible deammoniation during cycling lead to structural degradation.[30–34]

[a]*Key Laboratory of Photovoltaic and Energy Conservation Materials, CAS, Institute of Solid State Physics, Hefei Institutes of Physical Science, Chinese Academy of Sciences, Hefei, Anhui, 230031, P. R. China. E-mail: lemo@rntek.cas.cn, lhhu@rntek.cas.cn*
[b]*University of Science and Technology of China, Hefei, Anhui, 230026, P. R. China*
[c]*Hebei Computational Optical Imaging and Photoelectric Detection Technology Innovation Center, Hebei International Joint Research Center for Computational Optical Imaging and Intelligent Sensing, School of Mathematics and Physics Science and Engineering, Hebei University of Engineering, Handan, Hebei, 056038, P. R. China. E-mail: zhanghong81@hebeu.edu.cn*

To address these issues, the introduction of additional metal ions into the interlayer has been demonstrated to effectively stabilize the structure. Metal ions with lower electronegativity than vanadium can form stronger chemical bonds with oxygen, thereby reducing structural distortion.[35–37] Furthermore, the increased layer spacing provides extra ion diffusion pathways, which compensates for any potential decrease in specific capacity caused by metal ion doping.[38–40] Among various candidate metal ions (such as Ag^{+}, Na^{+}, K^{+}, Mg^{2+}, Ca^{2+}, Ce^{3+} and Rb^{4+}), Al^{3+} stands out with a high charge state, relatively large hydrated ion radius, moderate atomic weight, and strong Al–O bonds.[41–46] When Al^{3+} ions serve as interlayer pillar ions, they can effectively expand the interlayer spacing. Simultaneously, they suppress deammoniation through strengthened hydrogen bonding. The strong Al–O covalent bonds enhance structural stability by increasing shear resistance and restricting interlayer distortion.

In this study, we synthesized a nanobelt structured $NH_4V_4O_{10}$ material doped with Al^{3+} (denoted as Al-NVO) as a promising cathode for AZIBs. The nanobelt morphology of the cathode promotes increased contact between the active material and the electrolyte, thereby improving ion transport efficiency. The introduction of Al^{3+} ions enlarges the interlayer spacing, providing a smooth pathway for Zn^{2+} migration and ensuring favorable electrochemical kinetics. The pre-intercalated Al^{3+} ions act as pillars between layers, significantly enhancing structural stability and effectively suppressing irreversible deammoniation during cycling. The Al-NVO cathode delivers a high specific capacity of 460 mAh g^{-1} at 0.2 A g^{-1}, remarkable cycling stability (retaining 94.6% capacity after 2000 cycles at 5 A g^{-1}), and excellent rate performance (309 mAh g^{-1} at 10 A g^{-1}). The Al-NVO pouch cell achieves a capacity of 167 mAh g^{-1} with stability over 250 cycles, while a 0.6 Ah prototype battery sustains operation for more than 300 hours under deep cycling conditions. This work represents a significant advancement in the development of high-performance cathode materials for AZIBs. By addressing key challenges related to material stability and electrochemical performance, it paves the way for the practical application of AZIBs in large-scale energy storage scenarios.

2. Results and discussion

The crystalline structure and phase purity were systematically characterized using X-ray diffraction (XRD) analysis. As shown in Fig. 1a, all diffraction patterns are consistent with the pure monoclinic $NH_4V_4O_{10}$ phase (space group $C2/m$, JCPDS No. 31-0075).[43] This result confirms that Al^{3+} doping does not alter the crystal structure of NVO. The (001) diffraction peak in Al-NVO shows a slight shift towards lower angles compared to NVO, suggesting an expansion of the interlayer spacing from 9.9 Å to 10.2 Å due to Al^{3+} intercalation. X-ray photoelectron spectroscopy (XPS) analysis reveals changes in the chemical states induced by Al^{3+} doping. Both NVO and Al-NVO display characteristic V, O, N, and C peaks in their survey XPS spectra (Fig. S1a). An Al 2p peak is observed in Al-NVO (Fig. S1b), verifying the successful incorporation of Al^{3+} ions into the host structure. The high-resolution V 2p spectra (Fig. 1b) exhibit two characteristic oxidation states: V^{5+} at 517.9 eV and V^{4+} at 516.4 eV. Quantitative analysis indicates a higher V^{4+} proportion in Al-NVO (35%) compared to NVO (30%), suggesting partial reduction of V^{5+} *via* charge compensation during the incorporation of Al^{3+}.

The thermogravimetric (TG) curves of NVO and Al-NVO can be divided into three characteristic stages, as shown in Fig. 1c. Stage I (30–150 °C) corresponds to the elimination of physically adsorbed water, followed by Stage II (150–400 °C) involving the sequential loss of crystalline water and ammonium ions. Stage III (400–600 °C) represents complete ammonium ion decomposition accompanied by structural crystallization.[14] Although the total weight losses of Al-NVO and NVO are comparable (7.5% *vs.* 7.2%, respectively), indicating similar overall thermal decomposition behavior. The slightly higher total weight loss of Al-NVO is primarily attributed to the elimination of physically adsorbed water in the first stage (30–150 °C), which does not affect the intrinsic structural stability of the material. However, a critical distinction emerges in the second decomposition stage (150–400 °C), which corresponds to the loss of crystalline water and ammonium ions. Here, Al-NVO exhibits a 22% reduction in mass loss relative to NVO (4.2% *vs.* 5.4%). This significant difference directly demonstrates that Al doping stabilizes ammonium ions within the lattice framework by strengthening N–H···O hydrogen bonding, thereby suppressing irreversible deammoniation, a key factor for structural stability during cycling.

Energy-dispersive spectroscopy (EDS) analysis (Fig. 1d and Fig. S2) reveals the Al-doped sample maintains a V/Al atomic ratio of 1 : 0.14 while preserving the original N content (21.3% *vs.* 21.2% in pristine NVO). This, combined with TG data, confirms Al incorporation occurs without ammonium displacement, suggesting interlayer doping rather than cation substitution.

First-principles calculations were utilized to identify preferential Al^{3+} adsorption sites (Fig. 1e), demonstrating that site S1 exhibited the largest binding energy (−11.19 eV), indicating that Al^{3+} preferentially adsorbed at this site. For subsequent calculations of the energy barrier for zinc ion migration, we utilized a model where aluminum ions are adsorbed at site S1.

Elemental distribution mapping (Fig. S3 and S4) further confirms the successful incorporation of Al^{3+} ions. It also demonstrates the homogeneous dispersion of Al, N, V, and O throughout the Al-NVO architecture. Morphological characterization through scanning electron microscopy (SEM, Fig. 1f, g and Fig. S5a, b) and transmission electron microscopy (TEM, Fig. 1h and Fig. S5c) revealed preserved nanobelt morphology in both materials, confirming that Al^{3+} doping did not alter the morphology. High-resolution TEM analysis (Fig. 1i) showed an expanded interplanar spacing of 0.20 nm for the (004) plane in Al-NVO, compared to 0.19 nm in undoped NVO (Fig. S5d), which is consistent with XRD observations indicating lattice expansion.

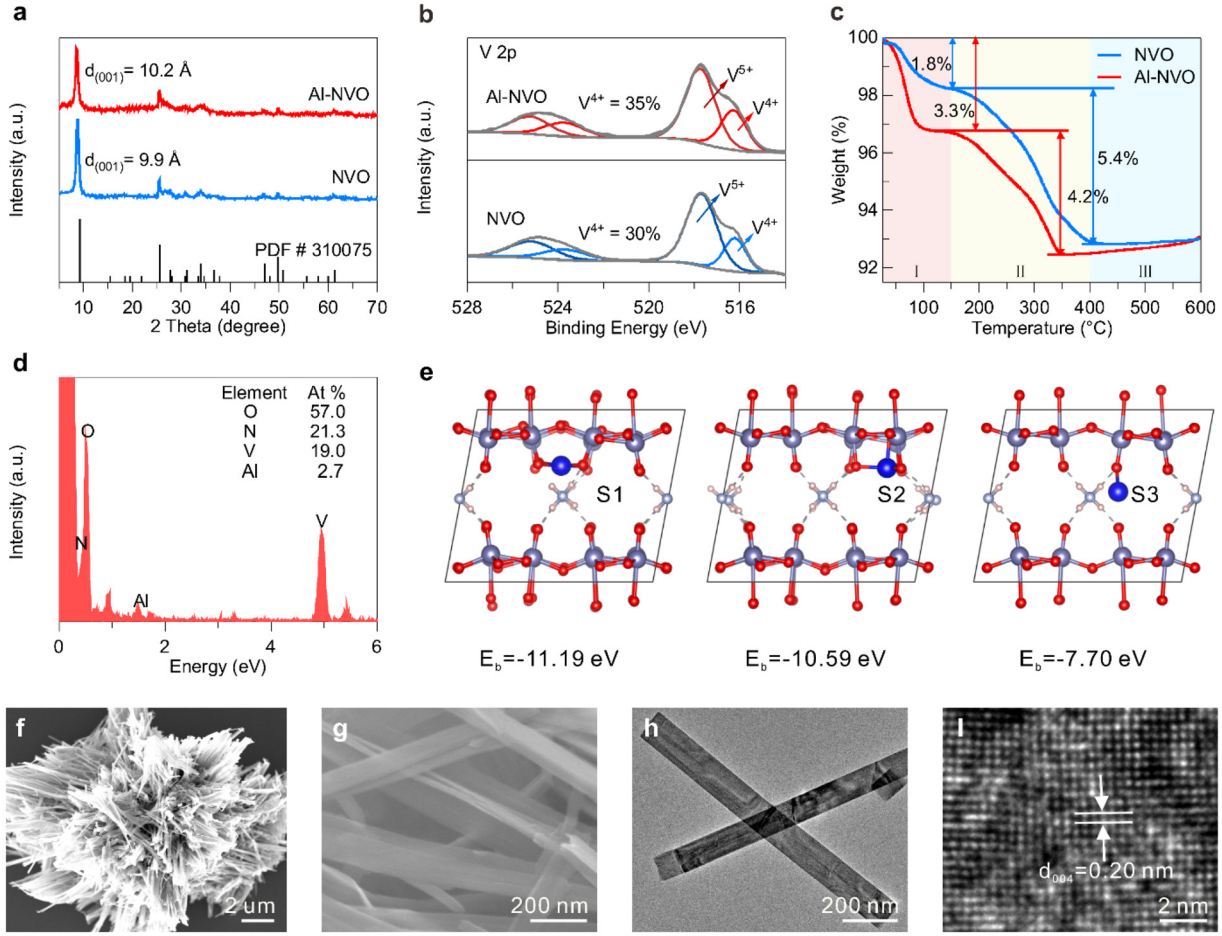

Fig. 1 Phase and structural analyses of Al-NVO and NVO (a) XRD patterns. (b) V 2p XPS spectra. (c) TG profiles under air atmosphere. (d) EDS of the Al-NVO. (e) Computational models and corresponding adsorption energies of Al atoms at three distinct lattice sites (S1–S3). (f and g) SEM, (h) TEM and (i) HR-TEM images of Al-NVO.

To investigate the electrochemical enhancement induced by Al^{3+} doping, AZIBs were assembled using Al-NVO/NVO cathodes, Zn metal anodes, and 3 M $ZnSO_4$ electrolyte. Fig. 2a and b respectively present the Cyclic voltammetry (CV) profiles of Al-NVO and NVO cathodes, recorded at a scan rate of 0.1 mV s^{-1} during the initial three cycles. The overlapped CV curves demonstrate the reversibility of the redox reactions, with characteristic peaks located at approximately 1.1 V (V^{5+}/V^{4+}) and 0.6 V (V^{4+}/V^{3+}), consistent with the reported vanadium-based cathodes.[41,42] A weak oxidation peak observed at around 1.45 V (highlighted by dashed black circles) can be attributed to irreversible deammoniation, in agreement with findings in prior studies.[31,47] Through comparative analysis, it is evident that the intensity of this peak in Al-NVO is significantly attenuated compared to that in NVO, indicating that Al^{3+} doping effectively suppresses irreversible deammoniation. Galvanostatic charge–discharge (GCD) profiles at 0.2 A g^{-1} (Fig. 2c and d) exhibit dual voltage plateaus at ~1.1 and ~0.6 V, corresponding to the CV redox couples and confirming a two-step Zn^{2+} insertion mechanism. The highly overlapped charging and discharging profiles of Al-NVO indicate superior reversibility compared to NVO. Moreover, Al-NVO attains a discharge capacity of 460 mAh g^{-1} at a current density of 0.2 A g^{-1}, which exceeds the 391 mAh g^{-1} observed for NVO.

The rate capability is presented in Fig. 2e and Fig. S6. As the current density increases from 0.2 to 10 A g^{-1}, the Al-NVO cathode exhibits specific capacities of 460, 451, 437, 418, 402, 388, 375, and 309 mAh g^{-1}, respectively. In contrast, under the same test conditions, the undoped NVO cathode delivers lower capacities of 391, 380, 370, 352, 338, 326, 314, and 257 mAh g^{-1} (Fig. S7). This concurrent improvement in capacity and rate performance underscores the effectiveness of Al^{3+} doping in enhancing the electrochemical performance of NVO.

Electrochemical impedance spectroscopy (EIS) analysis provides valuable mechanistic insights. The Al-NVO cathode displays a substantially reduced charge transfer resistance (R_{ct}), in contrast for the undoped NVO (Fig. 2f). The EIS spectra after 100 cycles (Fig. S8) show that Al-NVO retains a smaller charge transfer resistance compared to NVO. This indicates that Al^{3+} doping maintains efficient charge transfer even after prolonged cycling, reinforcing its role in enhancing dynamic stability. The decrease of R_{ct} after cycling may be attributed to

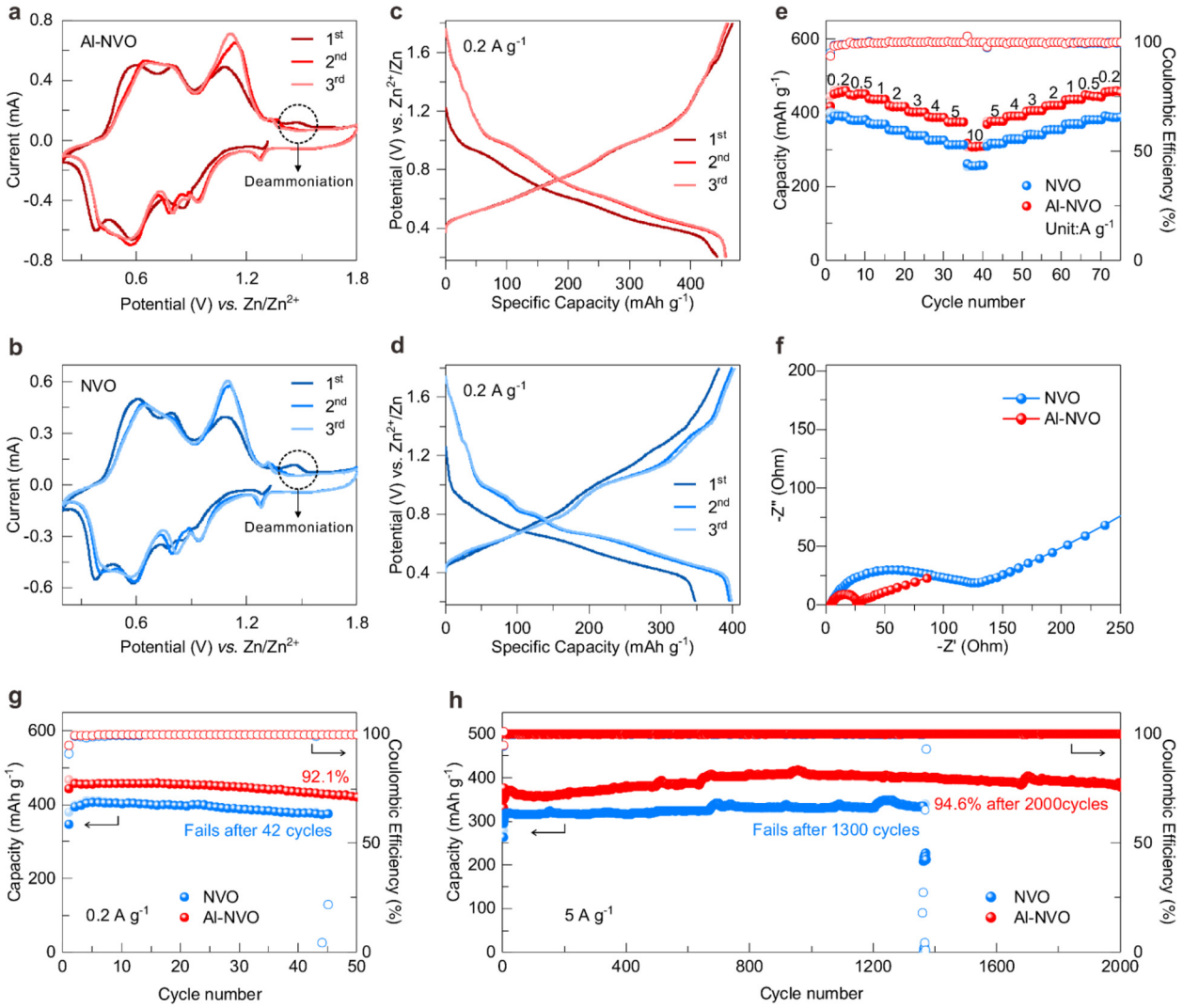

Fig. 2 Electrochemical characterization of Al-NVO and NVO cathodes. (a and b) CV profiles during the initial three cycles. (c and d) GCD curves at 0.2 A g^{-1}. (e) Rate performance across current densities (0.2–10 A g^{-1}). (f) Nyquist plots. Cycling stability at (g) 0.2 and (h) 5 A g^{-1}, respectively.

the electrode electrochemical activation. Evidently, Al^{3+} doping effectively enhances bulk electronic conductivity and facilitates ion diffusion.

To comprehensively understand the Zn^{2+} storage mechanisms in the Al-NVO system, CV analysis was conducted across scanning rates ranging from 0.2 to 1.2 mV s^{-1}. The CV profiles maintained their consistent shapes, with only minor shifts in the redox peaks due to polarization effects (Fig. S9). This consistency indicates the stable electrochemical behavior of the Al-NVO. Quantitative analysis through *b*-value determination yielded an average value of 0.80 (Fig. S10), suggesting a mixed Zn^{2+} storage mechanism comprising both surface-controlled capacitive processes and diffusion-limited intercalation reactions. Further deconvolution of current contributions revealed that the capacitive-dominated portion increased progressively from 69.3% to 84.6% with scanning rate elevation (Fig. S11–S14). This value exceeded that of the NVO cathode, demonstrating the enhanced capacitive performance of Al-NVO. The predominance of pseudocapacitive behavior at higher scan rates is a key factor underlying the superior rate capability of Al-NVO. Surface-controlled processes enable faster charge storage kinetics, allowing the electrode to respond rapidly to changing current demands. The enhanced capacitive contribution in Al-NVO can be rationally associated with the introduction of Al^{3+} ions, which are likely to induce structural modifications. These modifications promote interfacial charge storage while maintaining efficient bulk diffusion pathways.

The cycling stability of Al-NVO and NVO was compared in Fig. 2g, h and Fig. S15–S17. The Al-NVO cathode delivered an initial discharge capacity of 458 mAh g^{-1} at 0.2 A g^{-1}, retaining 422 mAh g^{-1} (92.1% capacity retention) after 50 cycles with minimal degradation. In contrast, the NVO cathode experienced significant structural degradation after only 42 cycles under identical testing conditions. At a high current density of

5 A g^{-1}, the Al-NVO cathode maintained 94.6% of its initial capacity after 2000 cycles, outperforming the NVO, which failed after 1300 cycles. This improvement in cycling stability can be attributed to the stabilizing effect of Al^{3+} doping. The doping mitigates the structural degradation caused by the repeated insertion and extraction of Zn^{2+} during charge and discharge processes, ensuring long-term electrochemical stability.

To gain more understanding of the Zn^{2+} storage mechanism in the Al-NVO cathode, *in situ* XRD analysis was performed during the first two electrochemical cycles (Fig. 3a and b). No additional new peaks were observed at fully charged or discharged states compared to the pristine cathode, confirming the phase purity retention during Zn^{2+} intercalation/deintercalation. The magnified XRD pattern (Fig. 3c) reveals a slightly high-angle shift in the (001) reflection at full discharge, corresponding to an interlayer spacing contraction from 10.2 Å to 9.9 Å (Fig. 3k). This lattice compression can be attributed to enhanced electrostatic interactions within the van der Waals gap resulting from Zn^{2+} intercalation. Upon charging to 1.8 V, the (001) diffraction peak returns to a larger interlayer spacing of 10.4 Å. During subsequent electrochemical cycling, the interlayer spacing of the (001) plane exhibits reversible variations between 9.9 Å and 10.4 Å, directly

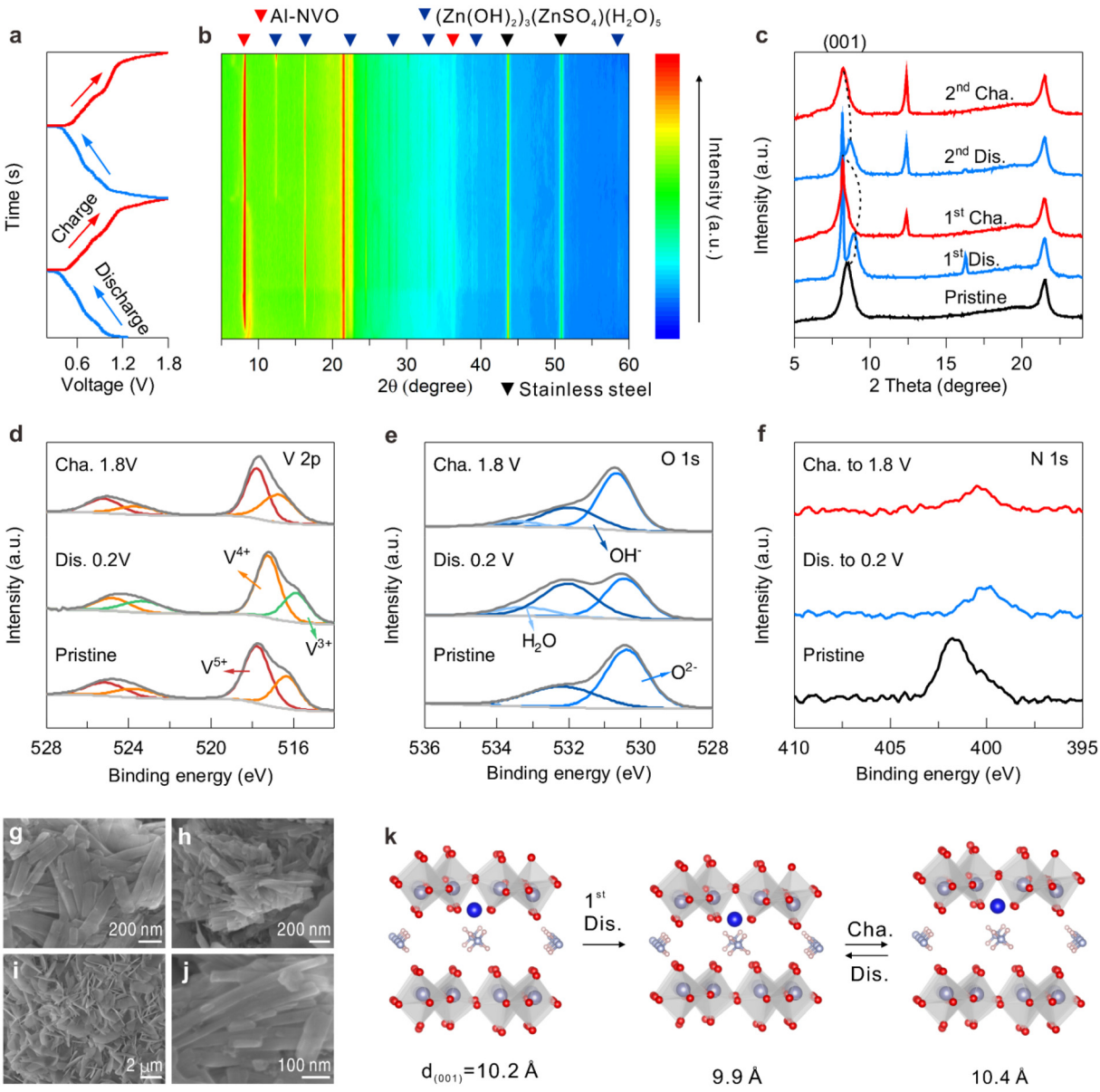

Fig. 3 Structural evolution of the Al-NVO cathode during Zn^{2+} storage. (a) Discharge/charge curve of at 0.2 A g^{-1}. (b) *In situ* XRD patterns collected during the first two cycles. (c) *Ex situ* XRD patterns of cycled electrodes. XPS spectra of (d) V 2p, (e) O 1s, and (f) N 1s at pristine, charged (1.8 V), and discharged (0.2 V) states. (g–j) SEM images obtained at pristine, discharged to 0.6 and 0.2 V, and charged to 1.8 V, respectively. (k) Schematic illustration of the reversible structural evolution of the Al-NVO cathode.

mirroring the Zn^{2+} insertion/extraction processes. This demonstrates the structural reversibility of the Al-NVO cathode during Zn^{2+} intercalation/deintercalation. New diffraction peaks at 8.1°, 16.2°, 24.4°, and 33.0° emerge in low voltage range, corresponding to $(Zn(OH)_2)_3(ZnSO_4)(H_2O)_5$ (JCPDS 78-0246), formed through OH^--mediated reactions as a common byproduct in $ZnSO_4$ electrolyte. These secondary phase signatures completely disappear upon recharging to 1.8 V, with the diffraction profile recovering its initial configuration. This reversible phase evolution, coupled with the dynamic yet stable adjustments of the (001) spacing, provides compelling evidence for the highly reversible Zn^{2+} (de)intercalation mechanism in the Al-NVO cathode.

XPS tests reveal critical electronic structure evolutions, as presented in Fig. 3d–f and Fig. S18–S23. The emergence of Zn $2p_{3/2}$ (1022 eV) and Zn $2p_{1/2}$ (1045 eV) signals after discharge confirms the successful intercalation of Zn^{2+} (Fig. S18). The redox activity of vanadium is evident from the V 2p spectrum. A new V^{3+} component at 515.3 eV indicates deep reduction, which vanishes entirely upon recharging (Fig. 3d), demonstrating the reversible V^{4+}/V^{3+} redox process. The O 1s spectral shows increased OH^- content (532.1 eV) during discharge (Fig. 3e), which is consistent with the formation of $(Zn(OH)_2)_3(ZnSO_4)(H_2O)_5$, as observed by XRD. NVO is similar to Al-NVO but has inferior reversibility and incomplete elimination of by-products (Fig. S19–S21). The Al 2p spectra (Fig. S22) maintain constant peak positions and oxidation state ratios throughout cycling, confirming Al^{3+} serves as a structural stabilizer rather than redox-active species. Comparative N 1s analysis (Fig. 3f *vs.* Fig. S23) reveals preserved N–H bonding in Al-NVO, demonstrating effective inhibition of deammoniation through Al^{3+} doping.

Morphological characterization (Fig. 3g–j and Fig. S24) corroborates the structural reversibility. Both the pristine and

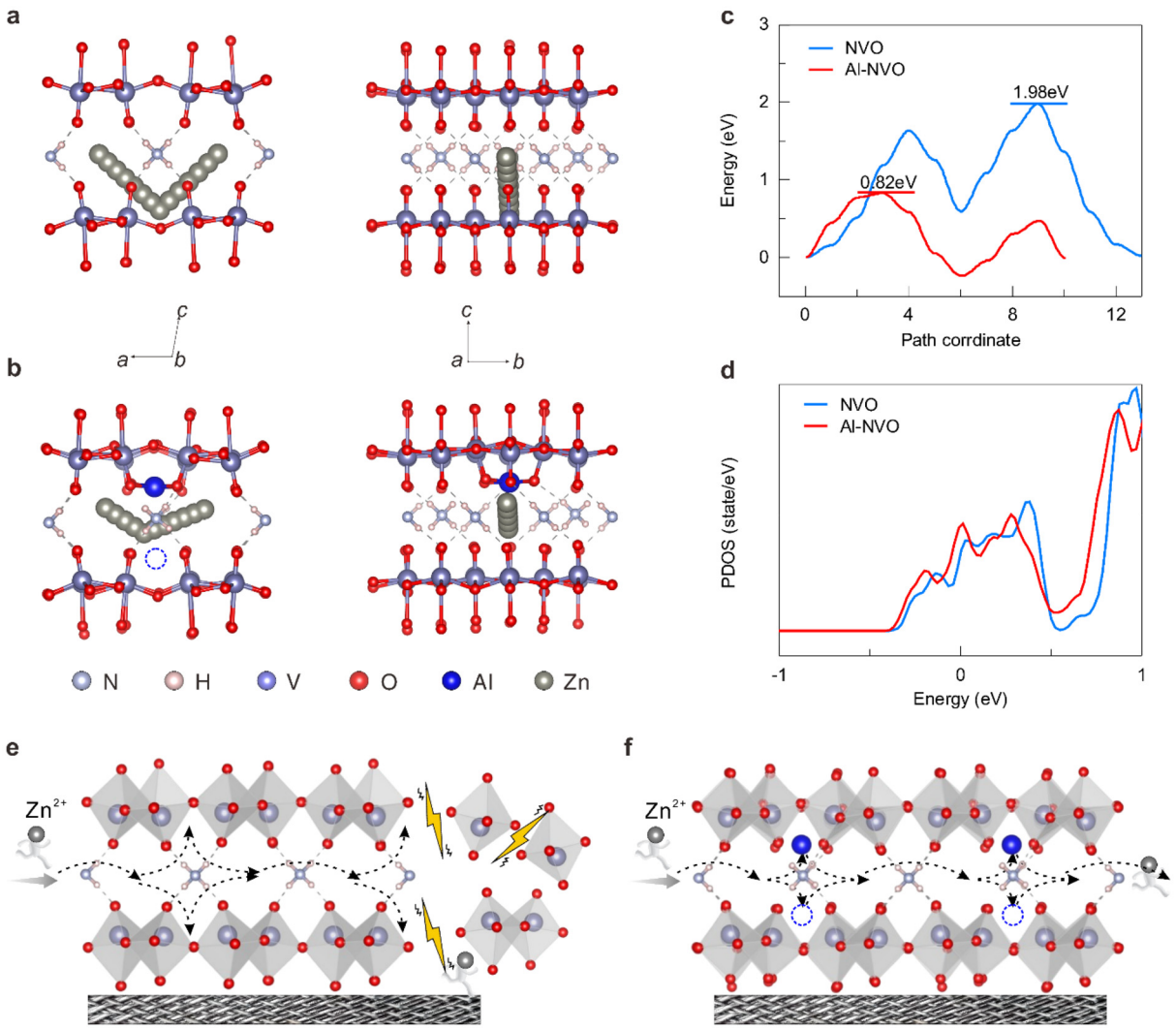

Fig. 4 DFT calculations: theoretical migration pathways for Zn^{2+} in (a) NVO and (b) Al-NVO. (c) Calculated Zn^{2+} diffusion barriers in NVO and Al-NVO cathodes. (d) DOS analysis for NVO and Al-NVO cathodes. Schematic diagrams comparing structural stability evolution of (e) NVO and (f) Al-NVO cathodes during electrochemical cycling.

charged states maintain smooth surfaces, while discharged samples exhibit sheet-like by-products identified as $(Zn(OH)_2)_3(ZnSO_4)(H_2O)_5$. These secondary phases dissolve completely upon recharging, as evidenced by the restoration of the surface morphology. The combined multiscale evidence, including crystallographic reversibility (XRD), electronic state recovery (XPS), and morphological restoration (SEM), establishes a comprehensive reaction mechanism (Fig. 3k). The XRD (Fig. S25) and SEM (Fig. S26) of Al-NVO after 100 cycles reveal that the (001) diffraction peak position and nanobelt morphology remain consistent with the pristine state, with no significant lattice distortion or structural collapse. In contrast, NVO shows obvious peak shifts and surface degradation, confirming that Al^{3+} doping 1effectively stabilizes the layered structure during repeated Zn^{2+} intercalation/deintercalation. In this mechanism, Al^{3+} ions act as pillars to stabilize the host structure, while enabling reversible Zn^{2+} storage through synergistic vanadium redox and interlayer spacing adjustments.

Density functional theory (DFT) calculations provided atomic-scale insights into the mechanistic function of Al^{3+} doping in optimizing Zn^{2+} diffusion kinetics and structural stability. The incorporation of Al^{3+} led to lattice expansion, as manifested by an increase in interlayer spacing (Δd = 0.3 Å *vs.* NVO). This structural modification widened the atomic separation between adjacent layers. As a result, the charge density was redistributed, effectively alleviating the electrostatic interactions between migrating Zn^{2+} ions and the V–O frameworks. As shown in Fig. 4a and b, the Zn^{2+} migration pathway in

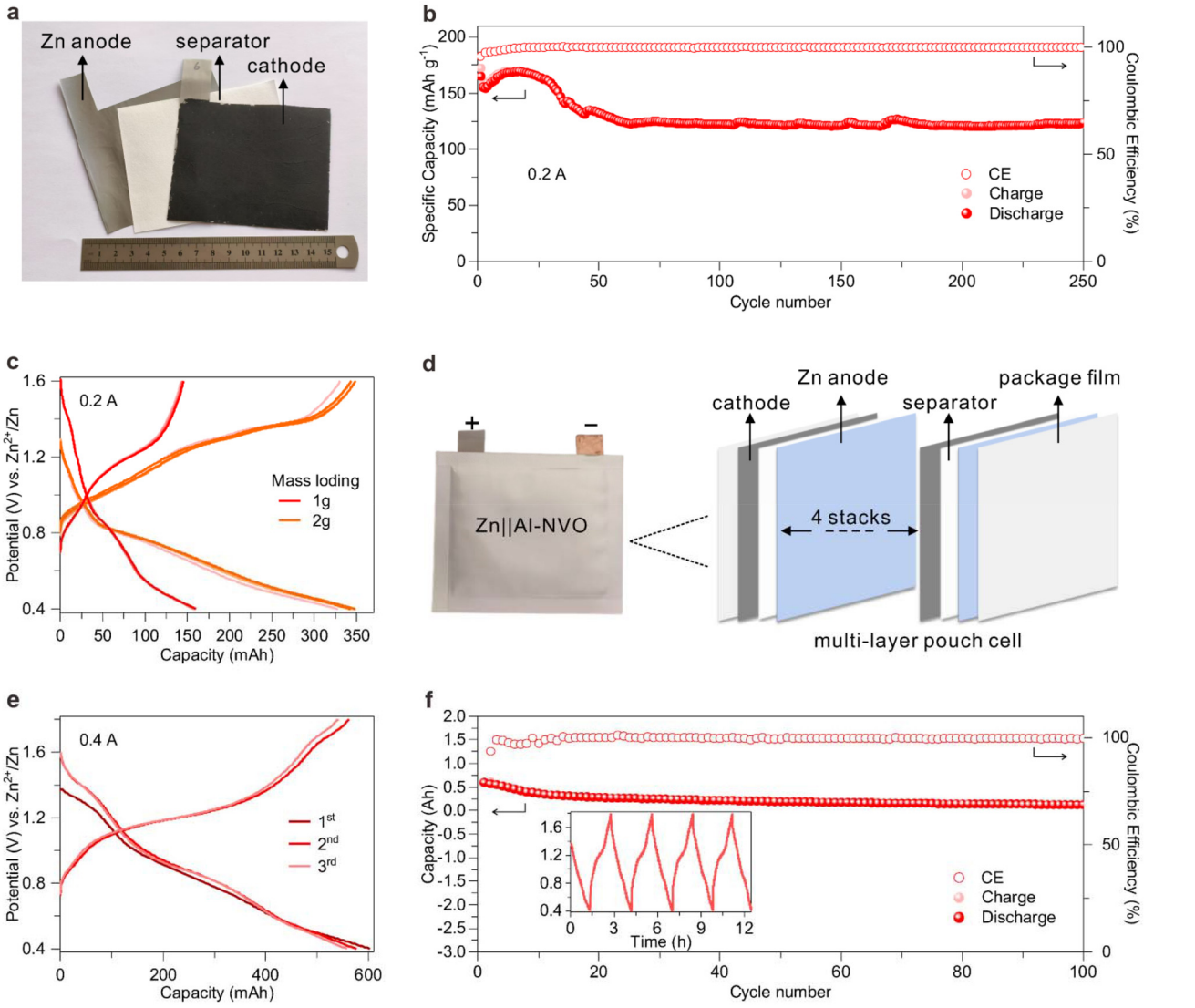

Fig. 5 Assembly process and electrochemical performance of Al-NVO//Zn pouch cells. (a) Photographic illustration of the essential components for pouch cell assembly, demonstrating the layered structure prior to encapsulation. (b) Cycling stability of the Al-NVO//Zn pouch cell operated at 0.2 A. (c) GCD curves of different mass loading at 0.2 A. (d) Schematic illustration of the configuration of a multi-layer Al-NVO//Zn pouch cell. (e) Voltage-capacity profiles of the multi-layer pouch cell with a substantial active material mass loading of 4.4 g and a current of 0.4 A. (f) Cycling performance of the multi-layer pouch cell.

Al-NVO was smoother compared to that in NVO. Notably, Al^{3+} ions located within the interlayers generate coulombic repulsive forces that partially counteract the Zn–O attraction, further facilitating cation mobility. The calculated migration barrier for Zn^{2+} decreased from 1.98 eV in NVO to 0.82 eV in Al-NVO (Fig. 4c), indicating a significant reduction in diffusion resistance. According to calculations of the Galvanostatic Intermittent Titration Technique (Fig. S27 and S28), the Zn^{2+} diffusion coefficient of the Al-NVO (10^{-8} cm^2 s^{-1}) is slightly higher than that of the NVO (10^{-9} cm^2 s^{-1}), suggesting the faster ion diffusion in the Al-NVO.

Electronic structure analysis through density of states (DOS) calculations (Fig. 4d) demonstrated enhanced metallicity in Al-NVO, with an increase in DOS near the Fermi level. This modification of the electronic structure corroborated the improved charge – transfer kinetics, which was consistent with the experimentally observed enhancements in rate capability.

Fig. 4e and f illustrated the stabilizing effect of Al^{3+} doping. During cycling, the NVO cathode underwent a progressive deamination process, with interlayer NH_4^+ playing a critical role in maintaining structural stability. Al-NVO preserved its structural integrity *via* two stabilizing mechanisms: first, the strong Al–O covalent bond ensured the overall structural stability. Second, the coulombic repulsion force generated by Al^{3+} ions redistributed the charge density. This weakened the electrostatic interactions between O^{2-} and Zn^{2+}, smoothing the migration pathway of Zn^{2+} and contributing to the long-term structural stability of Al-NVO.

To evaluate the practical application potential of the Al-NVO cathode, a pouch cell was assembled using Zn foil as the anode, 3M $ZnSO_4$ as the electrolyte, and Al-NVO as the cathode. Fig. 5a displays a photograph of the Zn anode, separator, and Al-NVO cathode. The electrode assembly had an active area of 80 cm^2, with a mass loading of ~1 g for the Al-NVO material. The GCD profiles from the 1st to the 20th cycles at 0.2 A (Fig. S29) revealed minimal capacity fade, with voltage plateaus remaining stable throughout these cycles. As expected, the cell provides an impressive specific capacity of 167 mAh g^{-1}. Long-term cycling tests (Fig. 5b and Fig. S30) further demonstrated exceptional electrochemical stability, retaining a discharge capacity of 125 mAh g^{-1} after 250 cycles at 0.2 A. When the mass loading of the Al-NVO active material was increased to 2 g, the discharge capacity of the pouch cell reached 350 mAh (Fig. 5c). This achievement is relatively rare in current reports (Table S1). To further demonstrate its practical applicability for grid-scale energy storage, an ampere-hour-level pouch cell was fabricated with a multi-layer architecture (3 cathode sheets paired with 2 anode sheets, as shown in Fig. 5d). This multi-layer stacked pouch cell provided an initial discharge capacity of 600 mAh (Fig. 5e), accompanied by an energy output of 492 mWh (Fig. S31) at 0.4 A, corresponding to a specific capacity of 136 mAh g^{-1} based on the total cathode active material mass (4.4 g). Notably, the multi-layer pouch cell exhibited robust cycling stability, sustaining over 100 cycles at a high current of 0.4 A while maintaining continuous operation for more than 300 hours (Fig. 5f). Collectively, these results underscore the practical feasibility of Al-NVO for large-scale energy storage, achieving a balance between high capacity, long lifespan, and scalability.

3. Conclusion

This work demonstrates that an Al^{3+} ions doping $NH_4V_4O_{10}$ (chemical formula: $Al_{0.56}NH_4V_4O_{10}$) exhibits competitive electrochemical performance as a cathode material for AZIBs. The Al-NVO cathode delivers a high specific capacity of 460 mAh g^{-1} at 0.2 A g^{-1} and excellent cyclability, maintaining 94.6% capacity retention after 2000 cycles. The Al-NVO-based pouch cell achieves a capacity of 167 mAh g^{-1} with stability over 250 cycles, while a 0.6 Ah prototype battery sustains operation for more than 300 hours under deep cycling conditions. Both experimental data and theoretical calculations elucidate three synergistic stabilization mechanisms: (1) Al^{3+} pillar ions expand the interlayer spacing while suppressing deammoniation through strengthened hydrogen bonding. (2) Strong Al–O covalent bonds enhance structural stability through increased shear resistance and reduced interlayer distortion. (3) Coulombic repulsion from Al^{3+} ions redistributes charge density, weakening the electrostatic interactions between O^{2-} and Zn^{2+}, thereby facilitating Zn^{2+} migration. *In situ* XRD and XPS analyses confirm a highly reversible Zn^{2+} storage mechanism with minimal structural changes. DFT calculations reveal optimized electron distribution and provide a low-energy-barrier pathway for Zn^{2+} migration (0.82 eV *vs.* 1.98 eV in NVO). This dual stabilization strategy, which involves simultaneously engineering ion transport channels and reinforcing host frameworks, offers valuable insights for developing high-performance cathodes in multivalent ion battery systems. It particularly addresses the critical challenges of structural degradation and sluggish kinetics in layered materials.

Author contributions

Yuqi Peng: writing – original draft, conceptualization, data curation, formal analysis, investigation, methodology. Li'e Mo: formal analysis, writing – review & editing. Weilin Yan: investigation, data curation. Lufan Liu: investigation. Xuejun Zhu: investigation. Yang Huang: writing – review & editing. Zhaoqian Li: writing – review & editing. Hong Zhang: formal analysis, software, funding acquisition. Linhua Hu: writing – review & editing, project administration, funding acquisition.

Conflicts of interest

There are no conflicts to declare.

Data availability

The data supporting this article have been included as part of the SI.

Details about the experimental synthesis, the characterization methods, and the DFT method; XPS spectra of the Al-NVO and NVO materials; EDS of the NVO; Elemental distribution mapping images; SEM, TEM and HR-TEM images of the NVO; GCD profiles of the Al-NVO and NVO cathode at various current densities; CV curves at different scan rates of the Al-NVO and NVO cathode; GCD profiles of the single-layer pouch cell with Al-NVO cathode; Comparison of the electrochemical performance for our work and some representative cathode materials in AZIBs. See DOI: **https://doi.org/10.1039/d5qi01280e**.

Acknowledgements

This work was supported by the Key Science and Technology Innovation Project of Anhui Province (202423i08050051), the Anhui Provincial Natural Science Foundation (2408085MB029), the HFIPS Director's Fund (YZJJGGZX202201). The Natural Science Foundation of Hebei Province of China (B2024402018). The numerical computation was performed on Hefei advanced computing center.

References

1 C. Li, S. Jin, L. A. Archer and L. F. Nazar, Toward practical aqueous zinc-ion batteries for electrochemical energy storage, *Joule*, 2022, **6**, 1733–1738.
2 J. Zhu, Z. Tie, S. Bi and Z. Niu, Towards More Sustainable Aqueous Zinc-Ion Batteries, *Angew. Chem., Int. Ed.*, 2024, **63**, e202403712.
3 L. Tang, H. Peng, J. Kang, H. Chen, M. Zhang, Y. Liu, D. H. Kim, Y. Liu and Z. Lin, Zn-based batteries for sustainable energy storage: strategies and mechanisms, *Chem. Soc. Rev.*, 2024, **53**, 4877–4925.
4 J. Zheng, Q. Zhao, T. Tang, J. Yin, C. D. Quilty, G. D. Renderos, X. Liu, Y. Deng, L. Wang, D. C. Bock, C. Jaye, D. Zhang, E. S. Takeuchi, K. J. Takeuchi, A. C. Marschilok and L. A. Archer, Reversible epitaxial electrodeposition of metals in battery anodes, *Science*, 2019, **366**, 645–648.
5 Y. Dai, R. Lu, C. Zhang, J. Li, Y. Yuan, Y. Mao, C. Ye, Z. Cai, J. Zhu, J. Li, R. Yu, L. Cui, S. Zhao, Q. An, G. He, G. I. N. Waterhouse, P. R. Shearing, Y. Ren, J. Lu, K. Amine, Z. Wang and L. Mai, Zn^{2+}-mediated catalysis for fast-charging aqueous Zn-ion batteries, *Nat. Catal.*, 2024, **7**, 776–784.
6 Y. Wang, L. E. Mo, X. Zhang, Y. Ren, T. Wei, Y. He, Y. Huang, H. Zhang, P. Tan, Z. Li, J. Zhou and L. Hu, Regulating Water Activity for All-Climate Aqueous Zinc-Ion Batteries, *Adv. Energy Mater.*, 2024, **14**, 2402041.
7 Z. Xiong, H. Sun, W. Su, W. Jin, H. Liu, Y. Huang and H. Liu, The Full-Graphdiyne-Based Fast-Charging Aqueous Zinc Ion Battery Toward Synergistically Boosted Capacity and Long Lifespan, *Small*, 2025, 2502191.
8 X. Jiang, K. Xiao, T. Hu, K. Yuan and Y. Chen, Aqueous eutectic electrolyte-derived organic/inorganic hybrid interphase towards reversible zinc electrochemistry for long-life zinc ion batteries, *Sci. China Mater.*, 2025, **68**, 1946–1958.
9 Y. Shang and D. Kundu, A path forward for the translational development of aqueous zinc-ion batteries, *Joule*, 2023, **7**, 244–250.
10 Y. Dai, X. Liao, R. Yu, J. Li, J. Li, S. Tan, P. He, Q. An, Q. Wei, L. Chen, X. Hong, K. Zhao, Y. Ren, J. Wu, Y. Zhao and L. Mai, Quicker and More Zn^{2+} Storage Predominantly from the Interface, *Adv. Mater.*, 2021, **33**, 2100359.
11 C. Shin, L. Yao, S.-Y. Jeong and T. N. Ng, Zinc-copper dual-ion electrolytes to suppress dendritic growth and increase anode utilization in zinc ion capacitors, *Sci. Adv.*, 2024, **10**, eadf9951.
12 X. Dou, X. Xie, S. Liang and G. Fang, Low-current-density stability of vanadium-based cathodes for aqueous zinc-ion batteries, *Sci. Bull.*, 2024, **69**, 833–845.
13 L. Hu, Z. Wu, C. Lu, F. Ye, Q. Liu and Z. Sun, Principles of interlayer-spacing regulation of layered vanadium phosphates for superior zinc-ion batteries, *Energy Environ. Sci.*, 2021, **14**, 4095–4106.
14 J. Kim, S. H. Lee, C. Park, H.-S. Kim, J.-H. Park, K. Y. Chung and H. Ahn, Controlling Vanadate Nanofiber Interlayer via Intercalation with Conducting Polymers: Cathode Material Design for Rechargeable Aqueous Zinc Ion Batteries, *Adv. Funct. Mater.*, 2021, **31**, 2100005.
15 H. Liu, H. Niu, W.-H. Huang, T. Shen, C. Li, C.-C. Chang, M. Yang, C. Gao, L. Yang, Q. Zong, Y. Pei, G. Cao and C. Liu, Unveiling the Local Structure and the Ligand Field of Organic Cation Preintercalated Vanadate Cathode for Aqueous Zinc-Ion Batteries, *ACS Energy Lett.*, 2024, **9**, 5492–5501.
16 X. X. Jia, C. F. Liu, Z. Wang, D. Huang and G. Z. Cao, Weakly Polarized Organic Cation-Modified Hydrated Vanadium Oxides for High-Energy Efficiency Aqueous Zinc-Ion Batteries, *Nano-Micro Lett.*, 2024, **16**.
17 Y. Zhang, Q. Li, W. Feng, H. Yue, S. Gao, Y. Su, Y. Tang, J. Wu, Z. Zhang, Y. Zhang, M. Shakouri, H.-C. Chen and H. Pang, Valence Engineering via Polyoxometalate-Induced on Vanadium Centers for Efficient Aqueous Zinc-Ion Batteries, *Angew. Chem., Int. Ed.*, 2025, e202501728.
18 D. Kundu, B. D. Adams, V. Duffort, S. H. Vajargah and L. F. Nazar, A high-capacity and long-life aqueous rechargeable zinc battery using a metal oxide intercalation cathode, *Nat. Energy*, 2016, **1**, 16119.
19 G. Zhang, T. Wu, H. Zhou, H. Jin, K. Liu, Y. Luo, H. Jiang, K. Huang, L. Huang and J. Zhou, Rich Alkali Ions Preintercalated Vanadium Oxides for Durable and Fast Zinc-Ion Storage, *ACS Energy Lett.*, 2021, **6**, 2111–2120.
20 Y. Xu, G. Fan, P. X. Sun, Y. Guo, Y. Wang, X. Gu, L. Wu and L. Yu, Carbon Nitride Pillared Vanadate Via Chemical Pre-

Intercalation Towards High-Performance Aqueous Zinc-Ion Batteries, *Angew. Chem., Int. Ed.*, 2023, **62**, e202303529.

21 Y. Zhang, Z. Li, L. Gong, X. Wang, P. Hu and J. Liu, Rational construction of Ag@MIL-88B(V)-derived hierarchical porous Ag-V_2O_5 heterostructures with enhanced diffusion kinetics and cycling stability for aqueous zinc-ion batteries, *J. Energy Chem.*, 2023, **77**, 561–571.

22 H. Tang, K. Wan, K. Zhang, A. Wang, M. Wang, J. Xie, P. Su, H. Dong, J. Sun and Y. Li, Realizing Dual-Mode Zinc-Ion Storage of Generic Vanadium-Based Cathodes via Organic Molecule Intercalation, *ACS Nano*, 2024, **18**, 30896–30909.

23 C. Zhang, Y. Huang, X. Xu, Z. Chen, G. Xiao, Y. Zhong, X. Wang, C. Gu and J. Tu, Bulk-to-surface co-modification of layered hydrated vanadate cathode for aqueous zinc ion batteries, *Energy Environ. Sci.*, 2024, **17**, 4090–4103.

24 M. Li, X. Liu, J. Wu, X. Dong, Y. Wang and S. Passerini, Efficient and Effective Synthesis of $CaV_6O_{16}{\cdot}2.7H_2O$ as High-Performance Cathode Material for Aqueous Zinc Metal Batteries, *Adv. Energy Mater.*, 2025, **15**, 2404037.

25 X. Hu, S. Gao, T. Lin, X. Peng, Y. Huang, Y. Zhang, X. Yang, L. Wang, G. Luo, Z. Wen, B. Johannessen, S. Wang, L. Wang and B. Luo, Iodine-Doped Sodium Vanadate Cathode for Improved Zn Ion Diffusion Kinetics, *Adv. Mater.*, 2025, 2416714.

26 M. Tamilselvan, T. V. M. Sreekanth, K. Yoo and J. Kim, Ultrathin ammonium vanadate nanoflakes on carbon fiber - A binder-free high-rate capability cathode for aqueous medium zinc ion storage, *J. Alloys Compd.*, 2021, **876**, 160130.

27 K. Fang, Y.-L. Liu, P. Chen, H. Zhang, D. Fang, H.-Y. Zhang, Z. Wei, L. Ding, G.-G. Wang and H. Y. Yang, Electrochemical activation strategy enabled ammonium vanadate cathodes for all-climate zinc-ion batteries, *Nano Energy*, 2023, **114**, 108671.

28 Z. Wu, J. Yao, C. Chen, X. Chen, X. Pan, J. Zheng, Y. Gan, J. Li, X. Liu, C. Xia, L. Lv, H. Wang and H. Wan, Ammonium intercalation engineering regulated structural stability of V_6O_{13} cathodes for durable zinc ion batteries, *Chem. Eng. J.*, 2024, **479**, 147889.

29 J. Zhang, R. Liu, C. Huang, C. Dong, L. Xu, L. Yuan, S. Lu, L. Wang, L. Zhang and L. Chen, Oxygen defect engineering and amphipathic molecules intercalation co-boosting fast kinetics and stable structure of S-doped $(NH_4)_2V_{10}O_{25}{\cdot}8H_2O$ free-standing cathode for aqueous Zn-ion storage, *Nano Energy*, 2024, **122**, 109301.

30 Q. Zong, W. Du, C. Liu, H. Yang, Q. Zhang, Z. Zhou, M. Atif, M. Alsalhi and G. Cao, Enhanced Reversible Zinc Ion Intercalation in Deficient Ammonium Vanadate for High-Performance Aqueous Zinc-Ion Battery, *Nano-Micro Lett.*, 2021, **13**, 116.

31 Y. Zheng, C. Tian, Y. Wu, L. Li, Y. Tao, L. Liang, G. Yu, J. Sun, S. Wu, F. Wang, Y. Pang, Z. Shen, Z. Pan, H. Chen and J. Wang, Dual-engineering of ammonium vanadate for enhanced aqueous and quasi-solid-state zinc ion batteries, *Energy Storage Mater.*, 2022, **52**, 664–674.

32 S. Kong, Y. Li, X. Zhang, Z. Xu, X. Wang, Y. Feng, W. Gong, C. Liu, K. Tian and Q. Li, Anchoring Polar Organic Molecules in Defective Ammonium Vanadate for High-Performance Flexible Aqueous Zinc-Ion Battery, *Small*, 2023, **19**, 2304462.

33 L. Chen, Y. Zheng, Z. Zhang, Y. Ma, Y. Wang, H. Xiao, M. Xu, Z. Li and G. Yuan, Optimizing ammonium vanadate crystal structure by facile in situ phase transformation of $VO_2/NH_4V_4O_{10}$ with special micro–nano feature for advanced aqueous zinc ion batteries, *Inorg. Chem. Front.*, 2024, **11**, 1266–1278.

34 S. Yao and Y. Sun, Defect engineering and morphology adjustment assist $NH_4V_4O_{10}$ to be a high-performance aqueous zinc ion battery cathode, *J. Mater. Chem. A*, 2024, **12**, 17213–17221.

35 Z. Deng, W. Shao, H. Wang, Y. Wang, J. Sheng, H. Mu, C. Lian and W. Wu, Augmenting specific capacitance of ammonium vanadate cathode in aqueous zinc-ion batteries via barium doping directed by glutamic acid, *J. Power Sources*, 2024, **614**, 234976.

36 T. He, S. Weng, Y. Ye, J. Cheng, X. Wang, X. Wang and B. Wang, Cation- deficient $Zn_{0.3}(NH_4)_{0.3}V_4O_{10}{\cdot}0.91H_2O$ for rechargeable aqueous zinc battery with superior low- temperature performance, *Energy Storage Mater.*, 2021, **38**, 389–396.

37 S. Zhao, S. Wang, J. Guo, L. Li, C. Li, Y. Sun, P. Xue, D. Wu, L. Wei, Y. Wang and Q. Zhang, Sodium-Ion and Polyaniline Co-Intercalation into Ammonium Vanadate Nanoarrays Induced Enlarged Interlayer Spacing as High-Capacity and Stable Cathodes for Flexible Aqueous Zinc-Ion Batteries, *Adv. Funct. Mater.*, 2023, **33**, 2305700.

38 L. M. Chen, Z. Q. Zhang, Y. Ma, Y. M. Wang, H. H. Xiao, M. Xu, Y. Y. Huang and G. H. Yuan, Tuning ionic conduction and structure stability of ammonium vanadate by intercalating polyaniline molecules for advanced aqueous zinc-ion batteries, *Inorg. Chem. Front.*, 2023, **10**, 1926–1937.

39 K. Wang, R. Yuan, M. Li, Y. Huang, W. Ai, Z. Du, P. He and B. Wang, Al^{3+} intercalated $NH_4V_4O_{10}$ nanosheet on carbon cloth for high-performance aqueous zinc-ion batteries, *Chem. Eng. J.*, 2023, **471**, 144655.

40 J. Chen, X. Zhang, Y. Li, X. Li, X. Zhang, Y. Chen, Q. Zheng, X. Wu, H. Zhang, X. Tan and D. Lin, Unlocking the Zn storage performance of ammonium vanadate nanoflowers as high-capacity cathodes for aqueous zinc-ion batteries via potassium ion and ethylene glycol co-intercalation engineering, *J. Mater. Chem. A*, 2024, **12**, 28119–28129.

41 Y. Qiu, Z. Sun, Z. Guo, J. Bi, G. Li and L. Qian, Oxygen-deficient $NH_4V_4O_{10}$ cathode with Ag quantum dots and interlayer Ag^+ towards high-performance aqueous zinc ion batteries, *Chem. Eng. J.*, 2024, **498**, 155765.

42 X. Wang, Y. Wang, A. Naveed, G. Li, H. Zhang, Y. Zhou, A. Dou, M. Su, Y. Liu, R. Guo and C. C. Li, Magnesium Ion Doping and Micro-Structural Engineering Assist $NH_4V_4O_{10}$ as a High-Performance Aqueous Zinc Ion Battery Cathode, *Adv. Funct. Mater.*, 2023, **33**, 2306205.

43 Q. Zong, Q. Q. Wang, C. F. Liu, D. W. Tao, J. Y. Wang, J. J. Zhang, H. W. Du, J. F. Chen, Q. L. Zhang and G. Z. Cao, Potassium Ammonium Vanadate with Rich Oxygen Vacancies for Fast and Highly Stable Zn-Ion Storage, *ACS Nano*, 2022, **16**, 4588–4598.

44 K. Wang, S. Li, X. Chen, J. Shen, H. Zhao and Y. Bai, Trifunctional Rb^{+}-Intercalation Enhancing the Electrochemical Cyclability of Ammonium Vanadate Cathode for Aqueous Zinc Ion Batteries, *ACS Nano*, 2024, **18**, 7311–7323.

45 L. Pan, Y. Sun, S. Yao, Y. Zhang and Z. Wen, Ce-doped $NH_4V_4O_{10}$ nanosheets anchored on carbon cloth: a high-performance cathode material for zinc-ion batteries, *J. Colloid Interface Sci.*, 2025, **699**, 138145.

46 W. Kang, B. Zhang, Z. Wang, Z. Zhang, M. Niu, X. An, Z. Mou, X. Fan, X. Hu, B. Xi and S. Xiong, Synchronous organic-inorganic co-intercalated ammonium vanadate cathode for advanced aqueous zinc-ion batteries, *J. Energy Chem.*, 2024, **94**, 608–617.

47 E. A. Esparcia Jr, M. S. Chae, J. D. Ocon and S.-T. Hong, Ammonium Vanadium Bronze ($NH_4V_4O_{10}$) as a High-Capacity Cathode Material for Nonaqueous Magnesium-Ion Batteries, *Chem. Mater.*, 2018, **30**, 3690–3696.